Supplement of Atmos. Chem. Phys., 26, 16047–16066, 2026
https://doi.org/10.5194/acp-26-16047-2026-supplement
© Author(s) 2026. CC BY 4.0 License.



Atmospheric Chemistry and Physics
Open Access

*Supplement of*

# Frequent occurrence of newly formed aerosol particles over wide geographical areas in the Arctic free troposphere and atmospheric boundary layer

**David J. Simon et al.**

*Correspondence to:* David J. Simon (simon@tropos.de)

The copyright of individual parts of the supplement might differ from the article licence.

## S1 Research flights during the aircraft measurement campaign

Fig. S1 shows the flight tracks of all eleven research flights (RFs) conducted with the Polar 6 (P6) aircraft during the measurement campaign "Boundary layer and Aerosol and Cloud Study in the Arctic, based on aircraft and T-Bird Measurements II" (BACSAM II).

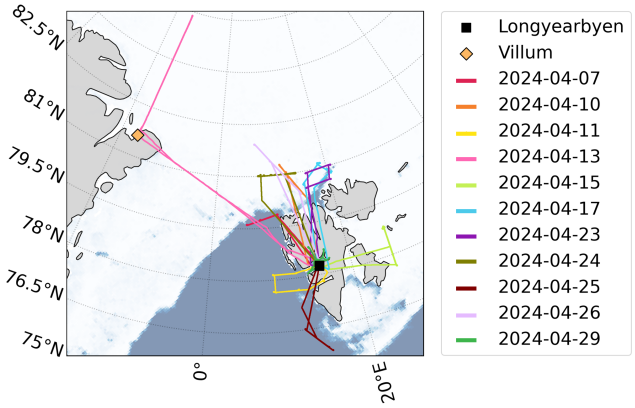



**Figure S1.** Flight tracks of all research flights during BACSAM II. The sea ice concentration is shown exemplary for 15 April 2024. The corresponding sea ice data were retrieved from www.seaice.uni-bremen.de (Spreen et al., 2008).

## S2 Correction for particle losses

To characterize particle losses in the sampling line from the aerosol inlet of the Polar 6 aircraft to the mobility particle size spectrometer (MPSS), we calculated the transmission efficiencies ($\eta = \eta(D_\mathrm{p})$, where $D_\mathrm{p}$ is the particle diameter) in the tubing utilizing the Particle Loss Calculator (Von der Weiden et al., 2009). The particle loss calculator includes losses due to diffusion, sedimentation, turbulent inertial deposition, and inertial deposition in bends and contractions. To approximate the aerosol particles' parameters, we assumed a density of $1.77\,\mathrm{g\,cm^{-3}}$, representing the density of ammonium sulfate particles, and a shape factor of 1, corresponding to spherical particles (Seinfeld and Pandis, 2006). As discussed in Sect. 2.2 of the main text, the flow in the sampling tubing is manually adjusted depending on the true airspeed of the aircraft (typically $tas \approx 60\ \mathrm{m\,s^{-1}}$ during flight section at low altitudes in the target regions, and $tas \approx 90\ \mathrm{m\,s^{-1}}$ during flight sections at high altitudes, e.g., transit flights). This procedure enables near-isokinetic sampling (Jurányi et al., 2025). Based on the corresponding flow recordings as well as pressure and temperature measurements of the MPSS throughout the campaign, for the loss calculations, pressure and temperature in the sampling line are set to the respective median values for measurements at high and low altitudes: $p_\mathrm{med} = 761\,\mathrm{hPa}$, $T_\mathrm{med} = 290\,\mathrm{K}$ for $tas \approx 90\ \mathrm{m\,s^{-1}}$, and $p_\mathrm{med} = 987\,\mathrm{hPa}$, $T_\mathrm{med} = 298\,\mathrm{K}$ for $tas \approx 60\ \mathrm{m\,s^{-1}}$. The calculations yield the transmission efficiency curves shown as solid lines in Fig. S2. To estimate the uncertainty in the transmission efficiencies associated with the median settings, we show the transmission efficiencies calculated for the 10th and 90th percentiles of the pressure and temperature distributions as shaded areas in Fig. S2 as well. Here, the respective parameters are set to $p_{10} = 678\,\mathrm{hPa}$, $T_{10} = 286\,\mathrm{K}$, $p_{90} = 905\,\mathrm{hPa}$, $T_{90} = 296\,\mathrm{K}$ for $tas \approx 90\ \mathrm{m\,s^{-1}}$, and $p_{10} = 862\,\mathrm{hPa}$, $T_{10} = 293\,\mathrm{K}$, $p_{90} = 1030\,\mathrm{hPa}$, $T_\mathrm{med} = 300\,\mathrm{K}$ for $tas \approx 60\ \mathrm{m\,s^{-1}}$.

For both typical true airspeeds of the aircraft, the transmission efficiencies calculated for the median pressure and temperature values range from $\approx 89\,\%$ at 10 nm over $\approx 95\,\%$ at 20 nm to $> 99\,\%$ at 100 nm (solid lines in Fig. S2). The values decrease towards smaller particle diameters to their minimum values at 10 nm as diffusional losses increase with decreasing particle size (Baron and Willeke, 2001, Fig. S2). Accordingly, we correct the MPSS-measured particle number size distribution (PNSD) data for particles losses in the sampling tubing by size-dependent correction factors ($c(D_\mathrm{p}) = 1/\eta(D_\mathrm{p})$) ranging from close to 1 to 1.12. Considering the transmission efficiencies calculated for the 10th and 90th percentiles, maximum differences are

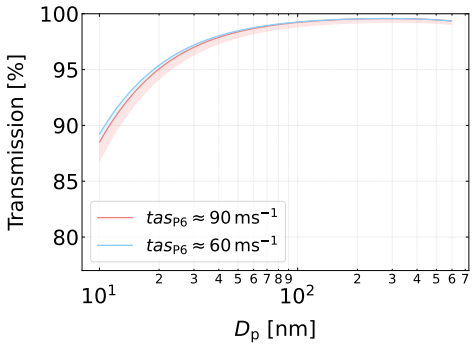



**Figure S2.** Particle size-dependent transmission efficiencies in the sampling tubing from the aerosol inlet to the MPSS for the two typical true airspeeds of the Polar 6 aircraft during the campaign.

$\approx 1\,\%$ for $tas \approx 60\ \mathrm{ms}^{-1}$ and $\approx 2\,\%$ for $tas \approx 90\ \mathrm{ms}^{-1}$ compared to the corrections based on the medians of the pressure and temperature distributions. We consider these errors to be negligible and apply the correction factors based on the median values to all PNSD data.

## S3 Atmospheric conditions along the aircraft's flight track

Due to the lack of, e.g., drop sonde and cloud microphysical measurements, data concerning the atmospheric stratification and the occurrence of clouds along the flight tracks are not continuously available. In other words, we cannot always unambiguously distinguish the airplane's position being within our outside the atmospheric boundary layer (ABL). Furthermore, we cannot always verify the presence or absence of clouds in the aircraft's proximity. However, we can provide a very rough estimate of the total measurement times inside the (cloud-free) ABL, in the (cloud-free) free troposphere, and in cloud vicinity based on reanalysis data from the fifth generation ECMWF reanalysis (ERA5) dataset. Thereto, we interpolated several ERA5 parameters such as specific cloud liquid water content ($CLWC$), specific cloud ice water content ($CIWC$), and the ABL height on to the flight track of the Polar 6 aircraft. Here, we consider a flight section to have been carried out in the vicinity of clouds if the sum of $CLWC$ and $CIWC$, i.e., the total cloud water content ($CWC = CLWC + CIWC$) exceeds the threshold of $CWC > 0.01\,\mathrm{g\,kg}^{-1}$. The latter is based on in situ measurements of $CWC$ of Arctic clouds conducted by McFarquhar and Cober (2004) in April 1998 and Moser et al. (2023) in April 2019. In both studies, values on the order of $CWC \sim 0.01\,\mathrm{g\,kg}^{-1}$ were reported for in-cloud measurements. We consider measurements to have taken place in the free troposphere (ABL) if the aircraft's flight altitude was above (below) the ERA5 ABL height. Here, the flight sections in cloud vicinity based on the threshold above are additionally excluded.

Based on the reanalysis data, for our campaign, we determine a total measurement time of about 25 hours and 10 minutes in the free troposphere, approximately 2 hours and 10 minutes in the vicinity of clouds, and about 8 hours and 10 minutes inside the ABL. Here, 60 minutes were carried out inside the ABL over ocean with sea ice floes, 3 hours and 30 minutes inside the ABL over sea ice, and 2 hours inside the ABL over open, completely ice-free ocean. In this analysis, the research flight on 29 April was omitted since it was carried out inside the fjords close to Longyearbyen under a completely closed cloud deck. These measurements amount to a duration of 1 hour and 40 minutes. Observations of newly formed particles on this day ($\approx$ 10 minutes) are assigned to the unclassified category.

The values reported above are associated with rather large uncertainties as they are are not well suited to describe the prevailing conditions at the aircraft's exact position. For example, not for all flight sections dedicated to probe directly the cloud top or cloud base, i.e., legs which are known to have taken place in the direct vicinity of clouds, ERA5 predicted consistently non-zero values of $CWC$ throughout the leg. Furthermore, during the case study on newly formed particles over sea ice, the ERA5-based ABL height was roughly 100 m lower than the ABL height determined from the vertical profiles of potential temperature derived from in situ measurements in the target region.

For the classification of measurement periods featuring newly formed particles to the categories "free troposphere", "cloud vicinity", "ABL over sea ice", and "ABL over ocean with sea ice floes", including all case studies, we only considered measurements for which the prevailing conditions could be unequivocally determined based on the in situ data. If newly formed particles were detected but the conditions could not unambiguously be identified (e.g., because the ABL height could not be determined for the target region, or because the absence/presence of clouds close to the aircraft could not be verified by studying in situ video and radiation data), these observations are assigned to the unclassified cases.

## S4 Thermodynamic conditions during the occurrence of newly formed particles

In Fig. S3, relative frequencies of occurrence of measured temperature and relative humidity pairs ($T$-$RH$ pairs) are plotted in a temperature vs. relative humidity plane. The relative frequencies were computed considering the number of measured $T$-$RH$ pairs during the presence of newly formed particles (Fig. S3a, 3686703 pairs) and considering the number of $T$-$RH$ pairs measured during the absence of newly formed particle (Fig. S3b, 9094434 pairs). The histograms shown in Fig. S3c-f were calculated by including the $T$-$RH$ data pairs recorded only during observations of newly formed particles in the free troposphere (Fig. S3c), only during observations of newly formed particles in the ABL over sea ice (Fig. S3d), only during observations of newly formed particles in the vicinity of clouds (Fig. S3e), and only during observations of newly formed particles in the ABL over ocean with sea ice floes (Fig. S3f). These data are then normalized by the data recorded during all observations of newly formed particles combined. That is, the normalization is the same as for the histogram depicted in Fig. S3a. The dotted horizontal and vertical lines separating the subplot into four quadrants in Fig. S3 are plotted to guide the eyes.
From Fig. S3, a clear pattern becomes visible. The data show three main clusters in the relative frequency distribution of temperature and humidity conditions during observations of newly formed particles (Fig. S3a), while the frequency distribution of $T$-$RH$ pairs measured during the absence of newly formed particles is broader, with fewer pronounced features (Fig. S3b). The peaks in Fig. S3a, i.e., in the $T$-$RH$ distribution measured during observations of newly formed particles, correspond to the different environmental scenarios under which newly formed particles were detected. Newly formed particles in the free troposphere were predominantly associated with cold and dry conditions (lower left quadrant in Fig. S3a, Fig. S3c). Newly formed particles in the ABL over sea ice occurred during cold and humid conditions (lower right quadrant in Fig. S3a, Fig. S3d). For newly formed particles detected in the vicinity of clouds, relatively warm and humid conditions prevailed (upper right quadrant in Fig. S3a, Fig. S3e). Similarly, newly formed particles inside the ABL over ocean with sea ice floes occurred during relatively warm, but less humid conditions compared to the observations in cloud vicinity (upper right quadrant in Fig. S3a, Fig. S3f). As the latter cases comprise only about 40 minutes of measurements (6 % of all observations of newly formed particles), the corresponding peaks in Fig. S3f are not strongly pronounced.
As mentioned in Sect. 3.1 in the main text and discussed comprehensively in supporting information (SI) Sect. S5, we found no clear indications of newly formed particles inside the ABL over open, completely ice-free ocean during our campaign. $T$-$RH$ data measured during such observations would likely also feature warm and humid conditions, similar to the data recorded during observations of newly formed particles in the vicinity of clouds and in the ABL over ocean with sea ice floes.
Altogether, these results show that newly formed particles observed during BACSAM II are associated with distinct thermodynamic conditions, which correspond to the different atmospheric scenarios for which newly formed particles were encountered. They include free tropospheric newly formed particles, newly formed particles inside the ABL over sea ice and over ocean with sea ice floes, as well as newly formed particles in the vicinity of clouds. These data provide important information on boundary conditions for laboratory experiments and modeling studies, both of which could facilitate the identification of nucleation mechanisms that might have lead to the presence of newly formed particles, and, furthermore, to assess the broader atmospheric (climate) impact of newly formed particles occurring throughout the lower Arctic troposphere.

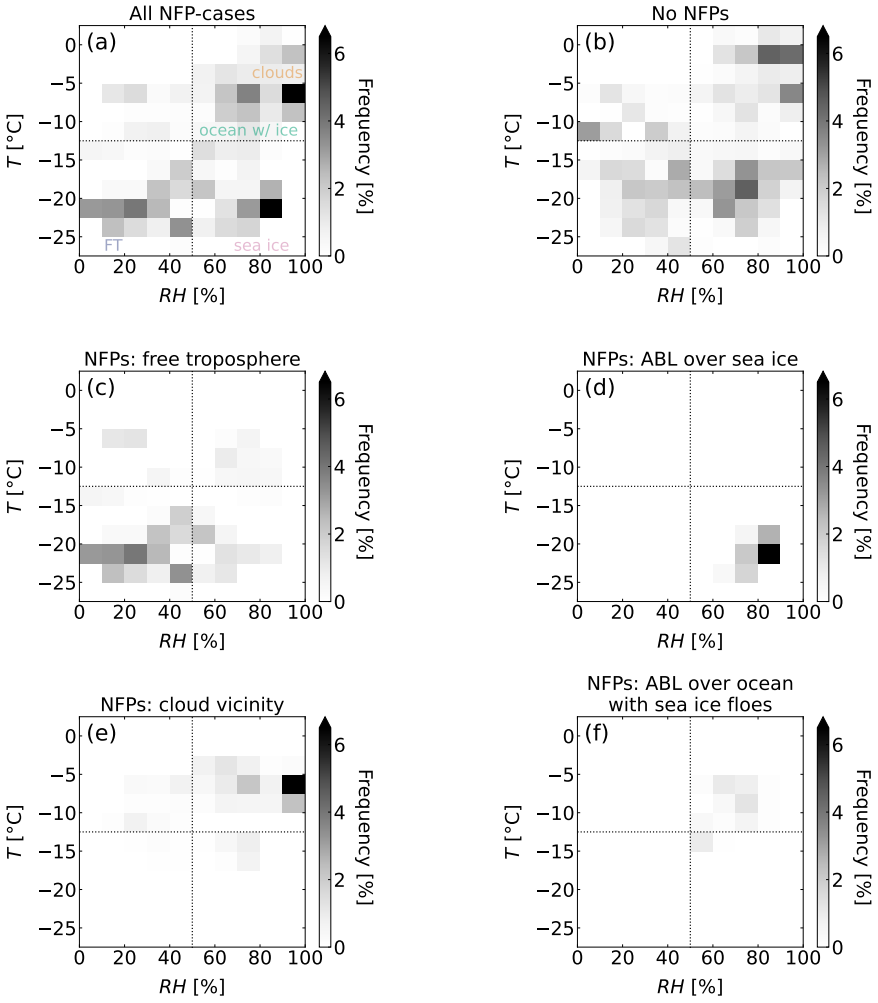



**Figure S3.** Temperature and relative humidity conditions during **(a)** newly formed particle-cases (NFP-cases) and **(b)** non-NFP-cases. The labels "FT", "sea ice", "clouds", and "ocean w/ ice" in panel (a) denote that within the corresponding quadrant, the measured temperature and relative humidity values are predominantly associated with newly formed particles observed in the free troposphere, the ABL over sea ice, cloud vicinity, and the ABL over ocean with sea ice floes, respectively. The second and third row depict temperature and relative humidity during the occurrence of newly formed particles **(c)** in the free troposphere, **(d)** the ABL over sea ice, **(e)**, the vicinity of clouds, **(f)** and the ABL over ocean with sea ice floes.

## S5 Newly formed particles inside the ABL over ocean with sea ice floes

### S5.1 Meteorological conditions

During the BACSAM II campaign, we conducted two research flights which included legs inside the ABL over ocean (on 11 and 25 April, Fig. S1). On all other days, the flight sections over open ocean visible in Fig. S1 were carried out above the ABL. On 11 April, we measured PNSDs in a target region in the lee west of Spitsbergen over ocean, with the ocean surface featuring both open water areas and patches of sea ice floes, as well as closed sea ice in the fjord in the proximity of WP7 (Fig. S4a). The air masses probed during the legs inside the ABL originated in sea ice-covered regions north and east of Svalbard (Fig. S4b,

c). In the last 24 hours prior to measurements inside the ABL, easterly winds advected cold air over the snow- and ice-covered Svalbard mountains to the target region over ocean (Fig. S4b, c). While mostly clear-sky conditions prevailed, a few scattered clouds were present in the eastern parts of the target region as well (Fig. S4a).

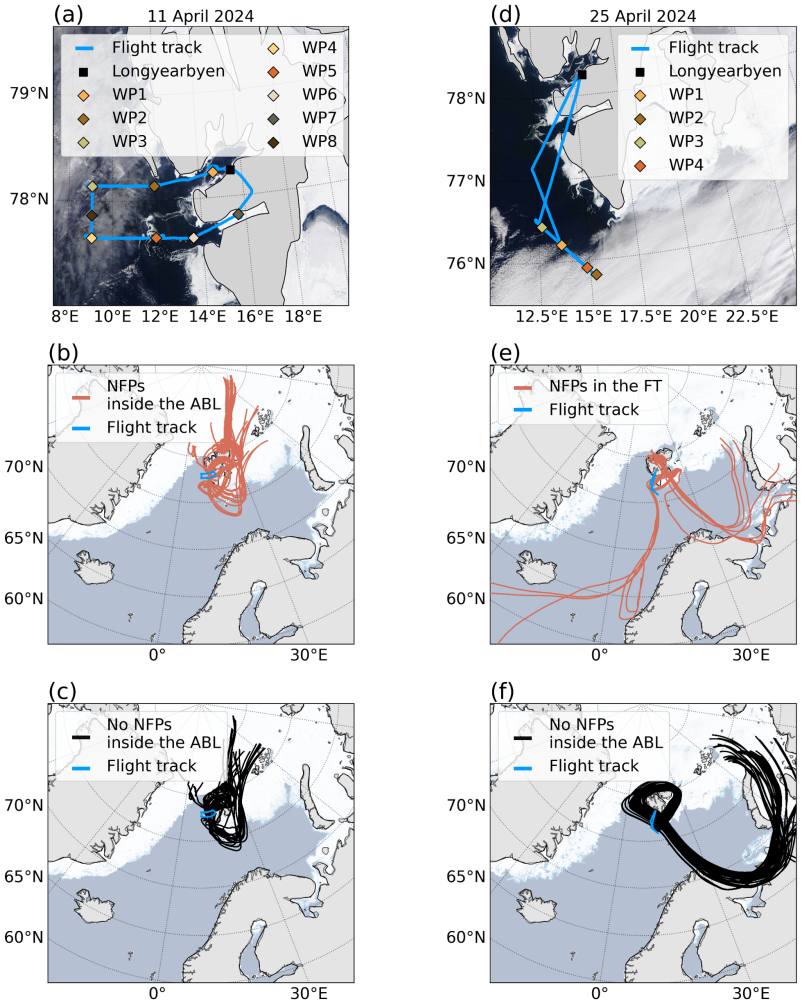



**Figure S4.** **(a)** Flight track of RF03 on 11 April 2024. **(b)** Five-day backward trajectories associated with newly formed particles (NFPs) inside the ABL on 11 April. **(c)** Five-day backward trajectories connected to PNSD measurements featuring no newly formed particles inside the ABL on 11 April. **(d)** Flight track of RF09 on 25 April 2024. **(e)** Five-day backward trajectories associated with newly formed particles in the free troposphere (FT) on 25 April. **(f)** Five-day backward trajectories connected to PNSD measurements featuring no newly formed particles inside the ABL on 25 April. The MODIS-TERRA satellite images shown in the panels (a) and (d) were retrieved from https://wvs.earthdata.nasa.gov. The sea ice concentration data shown in the subplots (b), (c), (e) and (f) were retrieved from www.seaice.uni-bremen.de (Spreen et al., 2008).

On 25 April, measurements were carried out in a target region southwest of Spitsbergen over open, completely ice-free ocean (Fig. S4d). On this day, air masses approached from southern latitudes (Fig. S4e, f). For the air masses probed inside the ABL (Fig. S4f), an anti-cyclonic flow around Svalbard resulted in north-easterly winds and advection over the sea ice and subsequently over open ocean prior to measurements inside the ABL (Fig. S4f). Air masses probed inside the ABL in the northern section of the target region additionally flowed over the Spitsbergen mountains before approaching the area over open

water. In this northern section, sparse scattered cumuli clouds were present, while overcast conditions prevailed in the southern part (Fig. S4d).

### S5.2 Particle number size distribution measurements

On 11 April, we carried out flight legs inside the ABL at altitudes of approximately 75 m (from about 9:10 to 9:20 UTC) and 240 m (9:25 to 9:45 UTC) in the northern section of the target region between waypoint 2 (WP2) and WP3 (left y-axis in Fig. S5a, see Fig. S4a for the location of the WPs). One leg was conducted at ≈1300 m (9:50 to 10:05 UTC) outside the ABL in the free troposphere. A similar pattern was flown in the southern section between WP4, WP5, WP6 and WP7 (left y-axis in Fig. S5a, see Fig. S4a for the location of the WPs) with legs at ≈1300 m in the free troposphere (10:25 to 10:40 UTC) and inside the ABL at ≈240 m (10:50 to 11:05 UTC), ≈75 m (11:10 to 11:40 UTC), and again at ≈240 m (11:45 to 12:00 UTC). No sea ice was present in the northern section between WP2 and WP3 (Fig. S5a, right y-axis) as shown by surface temperatures below the aircraft of about 3°C. In the southern section between WP4, WP5, WP6, and WP7, the surface contained both open water, scattered sea ice floes, and closed sea ice. This is demonstrated by surface temperatures ranging from about 3°C over open water close to WP4, over −1.8°C close to WP5 and WP6, to −15°C in the fjord close to WP7 (Fig. S5a, right y-axis). As mentioned above, easterly winds prevailed, resulting in off-ice flow, i.e., the areas probed inside the ABL over open water between WP4 and WP5 were located downwind of the sea ice (see Fig. S4b, Fig. S5a).

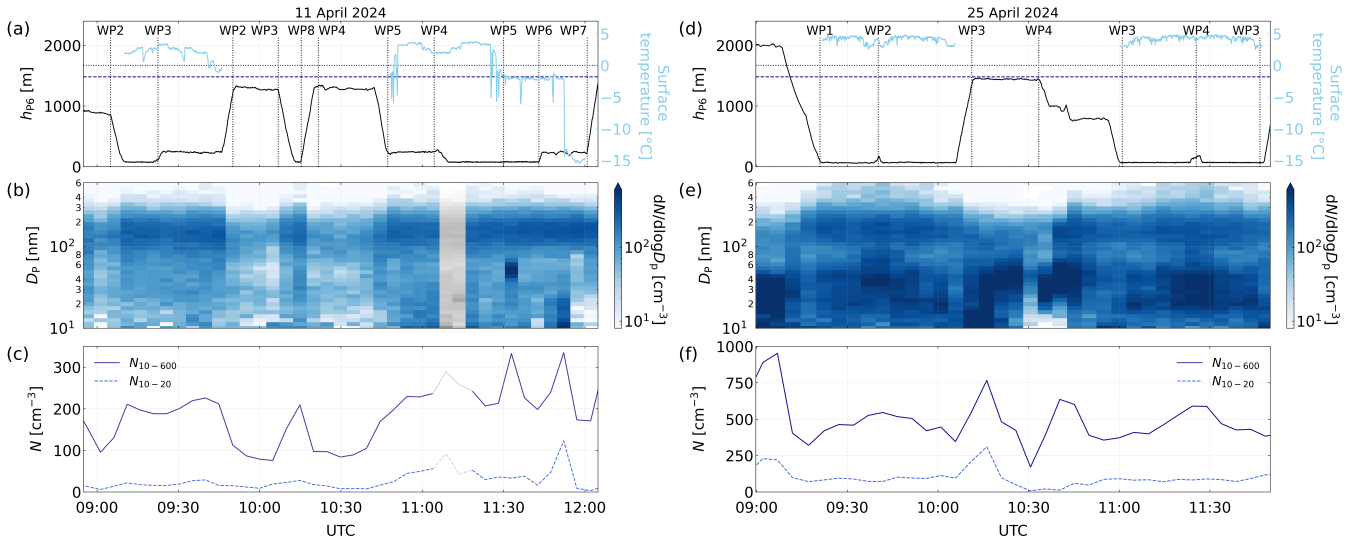



**Figure S5. (a)** P6 altitude during RF03 on 11 April 2024 (black line, left $y$-axis) as well as surface temperature (blue line, right $y$-axis). The dashed/dotted blue horizontal lines illustrate a surface temperature of 0°C and the freezing temperature of (salty) Arctic ocean water of −1.8°C. **(b)** MPSS-measured PNSD. The peak in the number concentrations $N_{10-600}$ around 11:32 UTC results from a pollution plume (likely ship exhaust) generating particles with a mode around 60 nm. The measurements from 11:05 to 11:15 UTC are grayed out because the exhaust of the Polar 6 research aircraft was sampled during the turn at WP4. **(c)** Integral particle number concentrations in the total measured size range ($10\ \mathrm{nm} \leq D_\mathrm{p} \leq 600\ \mathrm{nm}$, solid line) and in the nucleation mode size range ($10\ \mathrm{nm} \leq D_\mathrm{p} \leq 20\ \mathrm{nm}$, dashed line), respectively. **(d)** P6 altitude during RF09 on 25 April 2024 (black line, left $y$-axis) as well as surface temperature (blue line, right $y$-axis). The dashed/dotted blue horizontal lines illustrate a surface temperature of 0°C and the freezing temperature of Arctic ocean water of −1.8°C. **(e)** MPSS-measured PNSD. **(f)** Integral particle number concentrations in the total measured size range ($10\ \mathrm{nm} \leq D_\mathrm{p} \leq 600\ \mathrm{nm}$, solid line) and in the nucleation mode size range ($10\ \mathrm{nm} \leq D_\mathrm{p} \leq 20\ \mathrm{nm}$, dashed line), respectively. Note the different $y$-axis between the subplots (c) and (f).

In both the northern and the southern section, particle number concentrations in the size range from 10 nm to 600 nm were increased inside the ABL compared to the free troposphere (Fig. S5b, c). In the northern section, no newly formed particles during

the legs inside the ABL over completely ice-free ocean were present (Fig. S5b, c), as indicated by the absence of a prevailing distinct nucleation mode and rather low number concentrations in the size range from 10 nm to 20 nm ($N_{10-20} \approx 25\,\mathrm{cm}^{-3}$, $\approx 10\,\%$ of the total particle number concentrations measured in the range from 10 nm to 600 nm). One single PNSD measured at 9:30 UTC suggested the presence of a small nucleation mode with a maximum below 10 nm (Fig. S5b). However, because during this measurement a few scattered low-level clouds next to the aircraft were visible in the video data, but their distance to the aircraft could not be quantified and the leg was not carried out directly above/below the cloud top/base, this measurement is assigned to the unclassified category (see Fig. 2 and Fig. 3 in the main text and Sect. S3).

The number concentrations of particles in the nucleation mode size range from 10 nm to 20 nm increased by a factor of roughly two in the southern section inside the ABL over ocean with sea ice floes compared to the northern section (Fig. S5c). Here, $N_{10-20} \approx 50\,\mathrm{cm}^{-3}$, accounting for $\approx 20\,\%$ of the total particle number concentrations measured in the range from 10 nm to 600 nm. Several PNSDs showed a small but clear mode with a maximum below 10 nm (Fig. S5b, around 11:00, 11:15, 11:35, 11:45 UTC), indicative of the presence of newly formed particles. Interestingly, the largest nucleation mode (the highest peak in $N_{10-20}$) was observed directly at the transition between water with ice floes and closed sea ice in the fjord between WP6 and WP7 around 11:50 UTC (Fig. S5b). The median PNSDs for the legs inside the ABL are shown in Fig. S6 and will be discussed below.

On 25 April, four legs at altitudes of ≈67 m were carried out inside the ABL over open ocean (9:20 to 10:05 UTC and 11:00 to 11:45 UTC, Fig. S5d, left y-axis), i.e., with no sea ice present at all, as shown by sea surface temperatures of about $4^{\circ}$C (Fig. S5d, right y-axis). Additionally, one leg was flown at ≈1400 m in the free troposphere between WP3 and WP4 (10:10 to 10:35 UTC). Furthermore, one leg was carried out directly above the decreasing cloud top between WP3 and WP4 at altitudes between about ≈1000 m to ≈750 m (10:35 to 10:55 UTC). During the legs inside the ABL over open water, PNSDs showed no indications regarding the presence of a nucleation mode with a maximum below 10 nm, i.e., no indications of newly formed particles (Fig. S5e, f). In the free troposphere, around 9:00 UTC and 10:15 UTC, increased numbers of particles in the size range from 10 nm to 20 nm were present, and measured PNSDs indicated the presence of a pronounced nucleation mode. These newly formed particles in the free troposphere were associated with air masses from lower latitudes (Fig. S4e). However, we here focus on the measurements inside the ABL. The occurrence of newly formed particles in the free troposphere is discussed in detail in Sect. 3.2 in the main text.

A more detailed comparison of PNSDs measured during the legs inside the ABL over the Arctic ocean on 11 and 25 April is presented in Fig. S6. The accumulation mode concentrations are similar for all six median distributions depicted therein. Additionally, a sea salt mode was observed during the legs inside the ABL on 25 April (blue distribution in Fig. S6) due to sea spray aerosol (SSA) generation caused by strong winds (horizontal wind speeds of about $15\,\mathrm{ms}^{-1}$, strong fluctuations in vertical wind speeds; for a detailed case study on SSA fluxes on 25 April see Simon et al., 2025). The median PNSDs measured inside the ABL over completely ice-free ocean on 11 and 25 April featured no nucleation mode, i.e., no indications of the presence of newly formed particles were observed (blue and black distributions in Fig. S6). In contrast, PNSDs measured inside the ABL over ocean with sea ice floes indicated the presence of newly formed particles (red distributions in Fig. S6).

In summary, no evidence for the occurrence of newly formed particles during measurements inside the ABL over open, completely ice-free ocean was found. However, a small number of newly formed particles were detected during measurements inside the ABL over ocean with sea ice floes, i.e., in the direct vicinity and downwind of sea ice.

### S5.3 Chlorophyll-a concentration

We utilized satellite-derived Copernicus Global Ocean Colour data (Gohin et al., 2002; Hu et al., 2012) to carry out an analysis with respect to the chlorophyll-a (chl-a) mass concentration in the sea water during the measurements inside the ABL over ocean on 11 and 25 April. Here, chl-a is treated as a proxy for phytoplankton biomass (Siegel et al., 2013). It is well known that the aerosol precursor dimethylsulfide (DMS) results from the breakdown of dimethylsulfoniopropionate (DMSP), which is produced by phytoplankton (e.g., Simó, 2001; Willis et al., 2017). Thus, we assume that the chl-a concentrations are suited to investigate the potential for the release of DMS from the ocean surface to the atmosphere. In the Arctic at Ny-Ålesund, for example, Beck et al. (2021) showed a good agreement between measured chl-a and DMSP concentrations in seawater, which coincided with a rise in sulfuric acid (SA) and methane sulfonic acid (MSA), both of which are oxidation products of DMS, and the occurrence of new particle formation (NPF) and growth events.

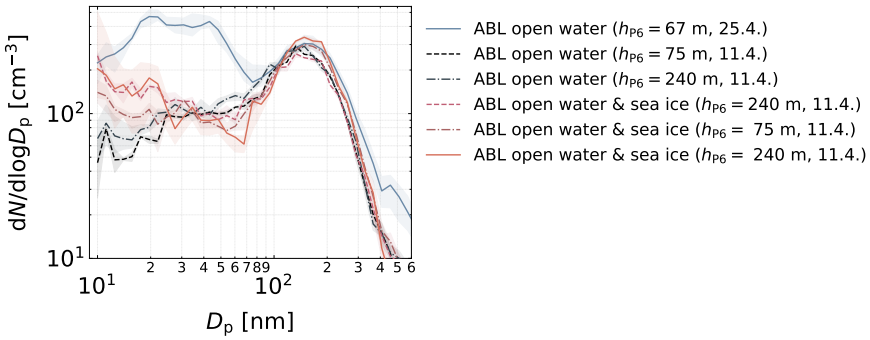



**Figure S6.** Median particle number size distributions during legs at constant altitude inside the ABL over completely ice-free open water (on 11 and 25 April, black and blue curves) and over ocean with both sea ice floes and open water areas present (on 11 April, red curves). The latter distributions over both open water and sea ice on 11 April are considered as indicative for newly formed particles. The shaded areas represent the interquartile ranges.

Compared to the background values close to zero, elevated chl-a concentrations are visible in the southern section of the target region on 11 April (Fig. S7a) where both open water and sea ice were present (Fig. S4a, S5a), suggesting that in the sea water in the area probed a phytoplankton bloom occurred. Furthermore, the data show no or only slightly increased chl-a concentrations in the northern section (Fig. S7a).

Fig. S7b depicts the backward trajectories inside the ABL on 11 April. We restrict the following discussion to air masses which resided inside the ABL since we expect that only those air masses could have picked up precursor gases from the ocean surface, whereas an influence of emissions from the surface on free tropospheric air masses is unlikely. Consequently, only the parts of the trajectories inside the ABL are shown in Fig. S7b-d, f-h. As mentioned above, easterly winds prevailed in both the northern and the southern section (Fig. S7b). The air masses sampled in the northern section, for which no newly formed particles were observed, did not pass over ocean surfaces featuring enhanced chl-a concentrations (Fig. S7b). In contrast, in the southern section, measurements in the direct vicinity of ocean waters with increased chl-a were conducted, as well as measurements downwind of these areas indicative of a phytoplankton bloom. On the two previous days, the air massed resided completely (10 April, Fig. S7c) and overwhelmingly outside of the ABL (9 April, Fig. S7d), limiting the possibility for precursor uptake from the (ocean) surface on those days. This suggests that the presumed emission of precursors, potentially leading to NPF and the occurrence of newly formed particles in the southern section of the target area on 11 April, occurred rather locally.

In the area probed on 25 April, the chl-a data showed no indications of a phytoplankton bloom (Fig. S7e). Similarly, in the areas where backward trajectories resided inside the ABL during 25 April and the two preceding days, no elevated chl-a concentrations were present in the sea water (Fig. S7f-h).

In summary, no evidence for a phytoplankton bloom in the northern section of the area probed on 11 April and in the area probed on 25 April was found based on the satellite data. However, in the southern section of the target region investigated on 11 April, the chl-a data suggest that a phytoplankton plume occurred. This might explain why newly formed particles were found inside the ABL over ocean with sea ice floes above and downwind of the plume area and the sea ice, but no newly formed particles were detected during the measurements inside the ABL over completely ice-free ocean. However, the occurrence of newly formed particles between WP6 and WP7 (Fig. S5a-c) upwind of the plume area on April 11 was likely not affected by the chl-a plume as the wind direction would prevent the eastward transport of possibly emitted precursors (Fig. S7b). Due to the absence of gas phase measurements, we cannot ultimately resolve if the potential release of precursors such as DMS from the sea surface and its possible participation in NPF might have contributed to the occurrence of newly formed particles on 11 April. Hence, we can only speculate that the presence of newly formed particles over ocean with sea ice floes on this day might be related to emissions of precursors from the open water or the sea ice, or both. Another potential explanation has been initially proposed by Leck and Bigg (1999, 2010) who suggested that the fragmentation of marine organic polymer gels led to the appearance of particles in the nucleation mode size range. Such events often involved the dissipation of cloud or fog

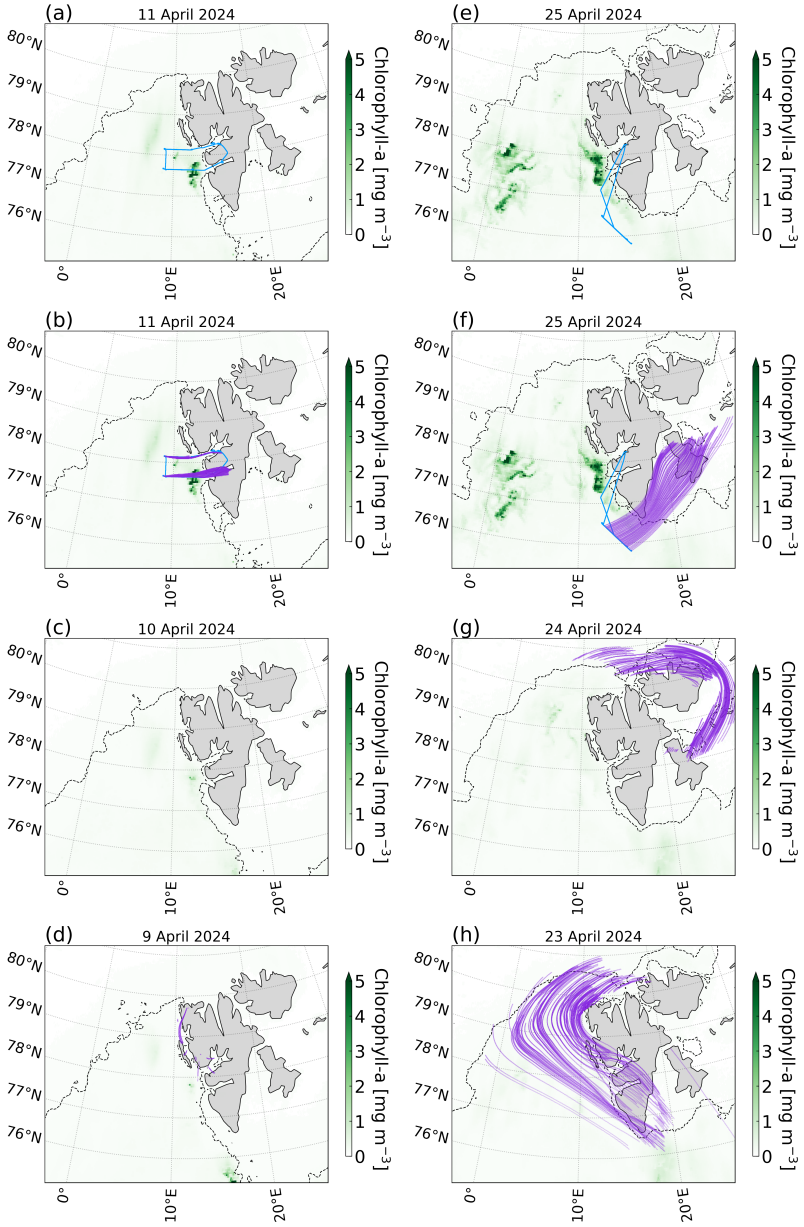



**Figure S7.** Flight track (blue), backward trajectories inside the ABL (violet), and chlorophyll-a mass concentrations (green) based on Copernicus-GlobColour data (Gohin et al., 2002; Hu et al., 2012) for the research flights featuring measurements inside the ABL over ocean on 11 and 25 April. The left column depicts the chlorophyll-a concentrations for 11 April 2024 and the two preceding days. Similarly, the right column depicts the chlorophyll-a concentrations for 25 April 2024 and the two preceding days. For convenience, only the respective flight tracks and chlorophyll-a concentrations for the days of the research flights are shown in the first row in panels (a) and (e). In the panels (b), (d), (d), (f), (g), and (h), the backward trajectories during the corresponding days are depicted as well. Only trajectories inside the ABL are shown, i.e., if no trajectory data are shown such as in panel (c) or gaps in the trajectories are visible such as in (d), (g), and (h), the trajectories did not reside inside the ABL at these geographical positions. The dashed black line in all subplots illustrates the sea ice extent based on 15 % sea ice concentration (Spreen et al., 2008).

droplets, emitting particles with sizes of a few nanometers to the atmosphere (Leck and Bigg, 1999, 2010; Karl et al., 2013; Leck et al., 2025).

## S6 New and recently formed particles in the free troposphere

Fig. S8 shows the median PNSD and corresponding interquartile range of all PNSD-measurements indicative of newly formed particles during the transit to Villum research station in the free troposphere (13 April 2024, RF04, Sect. 3.2 in the main text). These data were recorded during the time period 6:23 to 7:07 UTC and 7:17 to 7:40 UTC.
Two PNSDs measured in the time period from 7:07 to 7:17 UTC peaked at about 18 nm and showed no indications concerning a mode featuring a maximum below 10 nm (Fig. S8). According to our criteria defined in Sect. 2.2 in the main text, these PNSDs are not considered as indicative for newly formed particles. We rather interpret them as steming from "recent particle formation" (RPF), since the small particle sizes still suggest that these particles must originate from secondary particle production (e.g., Kulmala et al., 2004). Such recently formed particles are excluded from further analysis and we here focus solely on newly formed particles. Investigating recently formed particles in more detail is beyond the scope of this paper.

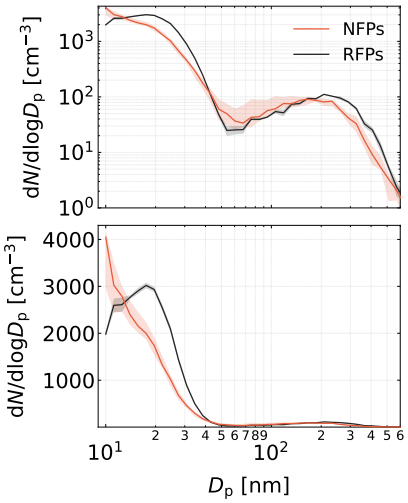



**Figure S8.** Median PNSD of measurements indicative of newly formed particles (NFPs) and recently formed particles (RFPs, solid lines) observed on 13 April 2024 during the transit from Longyearbyen to Villum Research Station (case study on newly formed particles in the free troposphere). The shaded areas represent the interquartile ranges.

## S7 Newly formed particles in the atmospheric boundary layer over sea ice

### S7.1 Sea ice conditions

To illustrate the sea ice conditions prevailing in the target region east of Svalbard between WP1 and WP3 on 15 April 2024 (RF05, Sect. 3.3 in the main text), Fig. S9 displays examples of fisheye camera images facing downward from the P6 aircraft during the legs inside the ABL. Leads and cracks in the sea ice are visible.

### S7.2 Vertical profile

From the inversion observed in the vertical profiles of potential temperature ($\Theta$) between WP1 and WP3, we determine the ABL height (Fig. S10). The solid line in Fig. S10 shows the mean $\Theta$-profile averaged over the four ascents/descents at WP1, WP2,

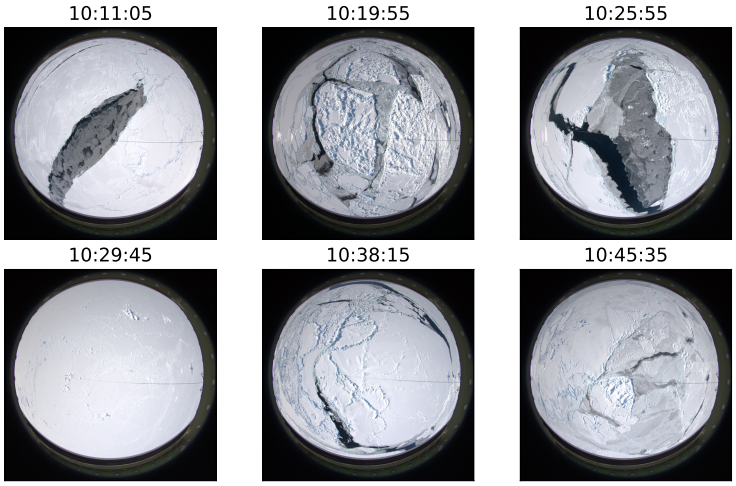



**Figure S9.** Sea ice conditions during RF05 on 15 April 2024 (case study in the ABL over sea ice). The title denotes the time in UTC.

and WP3 (see Fig. 8a in the main text). The shaded area represents the standard deviation and thus the variability between the individual ascents/descents. The data have been grouped into altitude bins with a width of 20 m before averaging. The markers with errorbars show mean values and standard deviations derived from the measurements during the horizontal legs. The horizontal dashed lines represent the average aircraft altitude during these low-level legs (at $\approx 70\,\mathrm{m}$ and $\approx 155\,\mathrm{m}$) close to the surface inside the ABL ($h_{\mathrm{P6,\,inside\,BL}}$) and the high-level leg above the ABL in the free troposphere ($h_{\mathrm{P6,\,outside\,BL}} \approx 850\,\mathrm{m}$). In Fig. S10, an inversion at an altitude of about 190 m can be identified for the target region.

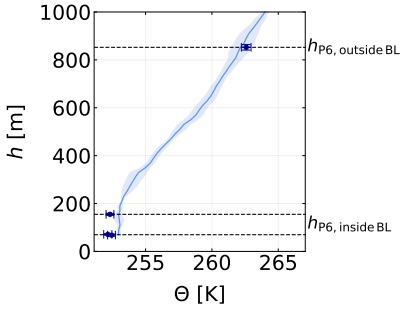



**Figure S10.** Mean vertical profile of potential temperature for the case study in the ABL over sea ice on 15 April 2024, derived from the ascents/descents (solid line). The shaded area represents the standard deviation. The markers with errorbars show mean values and standard deviations derived from the measurements during the horizontal legs. The horizontal dashed lines illustrate the average aircraft altitude during these legs.

### S7.3 Particle number size distributions

Fig. S11 shows the median PNSDs measured during the three consecutive legs carried out in the same area and at constant altitude between WP1 and WP3 (see Fig. 8a in the main text) inside the ABL over sea ice. ABL 1 refers to the first leg flown inside the ABL at an altitude of $\approx 70\,\mathrm{m}$ (10:15 to 10:47 UTC), ABL 2 to the second leg at $\approx 155\,\mathrm{m}$ (10:58 to 11:25 UTC), and ABL 3 to the third leg, again at $\approx 70\,\mathrm{m}$ (12:13 to 12:43 UTC). The decrease with time of the number concentration in the size range below 20 nm is clearly visible.

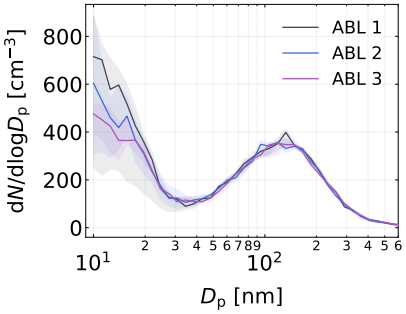



**Figure S11.** Median PNSDs (solid lines) and corresponding interquartile ranges (shaded areas) for the legs at ≈ 70 m (ABL 1 and ABL 3) and ≈ 155 m (ABL 2) inside the ABL over sea ice on 15 April 2024.

## S8 Newly formed particles in the vicinity of clouds

### S8.1 Sea ice conditions

To illustrate the sea ice conditions prevailing in the target region north of Svalbard between WP1 and WP2 on 24 April 2024 (RF08, Sect. 3.4 in the main text), Fig. S12 displays examples of fisheye camera images facing downward from the P6 aircraft during the leg at cloud base. Leads and cracks in the sea ice are visible.

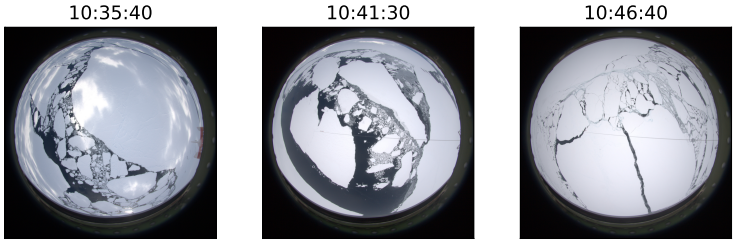



**Figure S12.** Sea ice conditions during RF08 on 24 April 2024 (case study in the vicinity of clouds). The title denotes the time in UTC.

### S8.2 Vertical profiles

For the case study on newly formed particles in the vicinity of clouds, the ascent through cloud (10:52 to 10:58 UTC, see Fig. 11a in the main text) is excluded from analysis with respect to the aerosol particle measurements, because erroneous measurements due to icing of the aerosol inlet and/or droplet shattering cannot be ruled out (Weber et al., 1998). Nevertheless, temperature and pressure data recorded during the ascent can with caution be used to determine vertical profiles of potential temperature to investigate the stratification in the target region. In Fig. S13, we show the potential temperature derived from these data collected during the ascent through cloud (see Fig. 11a in the main text). Directly in the target region between WP1 and WP2 (see Fig. 10a in the main text), no vertical profiling down to the lowest possible flight altitude was carried out. Therefore, in addition, the potential temperature derived from a vertical profile down to ≈ 80 m, which was conducted after passing WP2 and while returning toward the sea ice edge (see Fig. 10(a) in the main text), is depicted in Fig. S13. Here, the solid line represents the mean, averaged over ascent and descent, and the shaded area the corresponding standard deviation. Additionally, we show the potential temperature profile in the target region between WP1 and WP2 based on Copernicus Arctic Regional Reanalysis (CARRA) data. Cloud top and base, illustrated by the shaded gray area representing the cloud in Fig. S13, were determined from the profile of potential temperature and from in situ video data. Both CARRA and in situ data show an

inversion below the cloud, which suggests that in the area probed between WP1 and WP2, the clouds were decoupled from the surface.

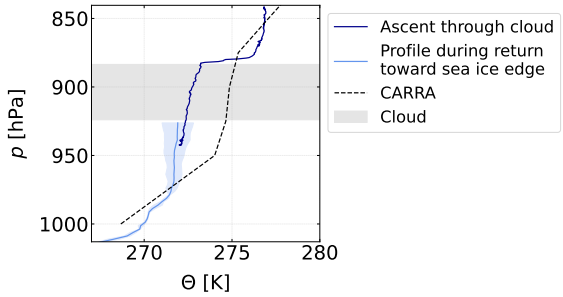



**Figure S13.** Vertical profile of potential temperature for the case study in the vicinity of clouds on 24 April 2024, derived from in situ data collected during ascents/descents (solid lines) as well as based on CARRA reanalysis data (dashed line).

### S8.3 Cloud top radiative cooling

We further utilize the ascent through the cloud to determine the radiative heating/cooling rates in an atmospheric layer between two flight altitudes, with $z_{\mathrm{bottom/top}}$ denoting the altitudes at the bottom/top of this layer (Lonardi et al., 2024). Following Lonardi et al. (2024), we calculate the heating/cooling rates as

$$\zeta = \frac{1}{\rho c_{\mathrm{p}}} \frac{F_{\mathrm{net}}(z_{\mathrm{top}}) - F_{\mathrm{net}}(z_{\mathrm{bottom}})}{z_{\mathrm{top}} - z_{\mathrm{bottom}}}, \tag{S1}$$

where $\rho$ and $c_{\mathrm{p}}$ are density and specific heat capacity at constant pressure of air, and $F_{\mathrm{net}}(z)$ the net thermal irradiance at flight altitude $z$. Positive/negative values in $\zeta$ indicate radiative heating/cooling (Lonardi et al., 2024). The heating/cooling rates are plotted in Fig. S14, which shows a sharp minium at about 1150 m, i.e., radiative cooling at the cloud top.

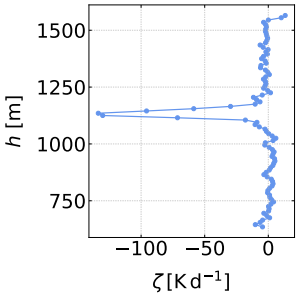



**Figure S14.** Radiative heating/cooling rates for the case study in the vicinity of clouds on 24 April 2024, determined from the ascent through cloud.

*Data availability.* Master tracks are available on PANGAEA for all research flights of the BACSAM II campaign (Jurányi et al., 2024). Backward trajectory data are available on PANGAEA for all research flights of the BACSAM II campaign (Kirbus and Wendisch, 2024). PNSD data from all research flights of the BACSAM II campaign are available on PANGAEA (Simon et al., 2026). Sea ice data were retrieved from www.seaice.uni-bremen.de (Spreen et al., 2008). MODIS-TERRA satellite images were retrieved from https://wvs.earthdata.nasa.gov. This study has been conducted using E.U. Copernicus Marine Service Information; https://www.doi.org/10.48670/moi-00281.

*Author contributions.* DJS participated in the data collection and flight planning during the BACSAM II campaign, analyzed and interpreted the data, and wrote the manuscript. JS participated in the data collection and flight planning, discussed the data, and contributed to the writing. JH participated in the data collection and flight planning, and processed the position, nose boom, and humidity data. BK performed the trajectory calculations and supported their analysis. JM participated in the data collection, flight planning, and calculated the radiative heating/cooling rates. ZJ, MH, BW, LK,AMJ, and MW participated in the flight planning, and the data collection and related discussions. KW was responsible for the development of the MPSS system. AH and ZJ functioned as PIs during the campaign. AH, ZJ, SH, GCR, MW, and MLP contributed to the discussion of the results. FS conceived the study, functioned as PI during the campaign, and contributed to data interpretation and writing. All authors read and edited the manuscript.

*Competing interests.* The authors declare no competing interests.

*Acknowledgements.* We gratefully acknowledge the funding by the Deutsche Forschungsgemeinschaft (DFG, German Research Foundation) – Project Number 268020496 – TRR 172, within the framework of the Transregional Collaborative Research Center "ArctiC Amplification: Climate Relevant Atmospheric and SurfaCe Processes, and Feedback Mechanisms (AC)$^3$", as well as the support of the Alfred-Wegener-Institute, Helmholtz Centre for Polar and Marine Research through grant number AWI_PA_02172. The authors used large language models (ChatGPT by OpenAI, Claude by Anthropic) solely to support coding tasks; all scientific reasoning, methodological decisions, analyses, and conclusions were developed independently by the authors.

## References


Baron, P. A. and Willeke, K.: Aerosol Measurement: Principles, Techniques, and Applications: [2001], John Wiley and Sons, 2001.

Beck, L. J., Sarnela, N., Junninen, H., Hoppe, C. J. M., Garmash, O., Bianchi, F., Riva, M., Rose, C., Peräkylä, O., Wimmer, D., Kausiala, O., Jokinen, T., Ahonen, L., Mikkilä, J., Hakala, J., He, X.-C., Kontkanen, J., Wolf, K. K. E., Cappelletti, D., Mazzola, M., Traversi, R., Petroselli, C., Viola, A. P., Vitale, V., Lange, R., Massling, A., Nøjgaard, J. K., Krejci, R., Karlsson, L., Zieger, P., Jang, S., Lee, K., Vakkari, V., Lampilahti, J., Thakur, R. C., Leino, K., Kangasluoma, J., Duplissy, E.-M., Siivola, E., Marbouti, M., Tham, Y. J., Saiz-Lopez, A., Petäjä, T., Ehn, M., Worsnop, D. R., Skov, H., Kulmala, M., Kerminen, V.-M., and Sipilä, M.: Differing mechanisms of new particle formation at two Arctic sites, Geophysical Research Letters, 48, e2020GL091 334, https://doi.org/10.1029/2020GL091334, 2021.

Gohin, F., Druon, J. N., and Lampert, L.: A five channel chlorophyll concentration algorithm applied to SeaWiFS data processed by SeaDAS in coastal waters, International Journal of Remote Sensing, 23, 1639–1661, https://doi.org/10.1080/01431160110071879, 2002.

Hu, C., Lee, Z., and Franz, B.: Chlorophyll aalgorithms for oligotrophic oceans: A novel approach based on three-band reflectance difference, Journal of Geophysical Research: Oceans, 117, https://doi.org/https://doi.org/10.1029/2011JC007395, 2012.

Jurányi, Z., Stratmann, F., Herber, A., Wendisch, M., and Borrmann, S.: Master tracks in different resolutions during POLAR 6 campaign P6-247_BACSAM2_2024, https://doi.org/10.1594/PANGAEA.971763, 2024.

Jurányi, Z., Lüpkes, C., Stratmann, F., Hartmann, J., Schaefer, J., Jörss, A.-M., Schulz, A., Wetzel, B., Simon, D., Gebhard, E., Stöhr, M., Hofmann, P., Kalmbach, D., Grawe, S., Wendisch, M., and Herber, A.: The T-Bird – a new aircraft-towed instrument platform to measure aerosol properties and turbulence close to the surface: introduction to the aerosol measurement system, Atmospheric Measurement Techniques, 18, 3477–3494, https://doi.org/10.5194/amt-18-3477-2025, 2025.

Karl, M., Leck, C., Coz, E., and Heintzenberg, J.: Marine nanogels as a source of atmospheric nanoparticles in the high Arctic, Geophysical Research Letters, 40, 3738–3743, https://doi.org/https://doi.org/10.1002/grl.50661, 2013.

Kirbus, B. and Wendisch, M.: Five-day backwards trajectories at one minute resolution along the flight tracks of the Polar 6 research aircraft during BACSAM II, https://doi.org/10.1594/PANGAEA.971694, 2024.

Kulmala, M., Vehkamäki, H., Petäjä, T., Dal Maso, M., Lauri, A., Kerminen, V.-M., Birmili, W., and McMurry, P.: Formation and growth rates of ultrafine atmospheric particles: a review of observations, Journal of Aerosol Science, 35, 143–176, https://doi.org/10.1016/j.jaerosci.2003.10.003, 2004.

Leck, C. and Bigg, E. K.: Aerosol production over remote marine areas-A new route, Geophysical Research Letters, 26, 3577–3580, https://doi.org/https://doi.org/10.1029/1999GL010807, 1999.

Leck, C. and Bigg, E. K.: New Particle Formation of Marine Biological Origin, Aerosol Science and Technology, 44, 570–577, https://doi.org/10.1080/02786826.2010.481222, 2010.

Leck, C., Heintzenberg, J., Nygård, T., and Naakka, T.: Is the summer aerosol over the Arctic controlled by regional atmospheric circulation or ice conditions? Trends and future implications, Atmospheric Chemistry and Physics, 25, 16 775–16 795, https://doi.org/10.5194/acp-25-16775-2025, 2025.

Lonardi, M., Akansu, E. F., Ehrlich, A., Mazzola, M., Pilz, C., Shupe, M. D., Siebert, H., and Wendisch, M.: Tethered balloon-borne observations of thermal-infrared irradiance and cooling rate profiles in the Arctic atmospheric boundary layer, Atmospheric Chemistry and Physics, 24, 1961–1978, https://doi.org/10.5194/acp-24-1961-2024, 2024.

McFarquhar, G. M. and Cober, S. G.: Single-scattering properties of mixed-phase Arctic clouds at solar wavelengths: Impacts on radiative transfer, Journal of Climate, 17, 3799–3813, https://doi.org/10.1175/1520-0442(2004)017<3799:SPOMAC>2.0.CO;2, 2004.

Moser, M., Voigt, C., Jurkat-Witschas, T., Hahn, V., Mioche, G., Jourdan, O., Dupuy, R., Gourbeyre, C., Schwarzenboeck, A., Lucke, J., Boose, Y., Mech, M., Borrmann, S., Ehrlich, A., Herber, A., Lüpkes, C., and Wendisch, M.: Microphysical and thermodynamic phase analyses of Arctic low-level clouds measured above the sea ice and the open ocean in spring and summer, Atmospheric Chemistry and Physics, 23, 7257–7280, https://doi.org/10.5194/acp-23-7257-2023, 2023.

Seinfeld, J. H. and Pandis, S. N.: Atmospheric chemistry and physics: from air pollution to climate change, John Wiley & Sons, ISBN 978-0-471-72018-8, 2006.

Siegel, D. A., Behrenfeld, M. J., Maritorena, S., McClain, C. R., Antoine, D., Bailey, S. W., Bontempi, P. S., Boss, E. S., Dierssen, H. M., Doney, S. C., et al.: Regional to global assessments of phytoplankton dynamics from the SeaWiFS mission, Remote Sensing of Environment, 135, 77–91, 2013.

Simó, R.: Production of atmospheric sulfur by oceanic plankton: biogeochemical, ecological and evolutionary links, Trends in Ecology & Evolution, 16, 287–294, 2001.

Simon, D. J., Hartmann, J., Schaefer, J., Zeppenfeld, S., Lüpkes, C., Hartmann, M., Wetzel, B., Heinold, B., Jurányi, Z., Schulz, A., et al.: Turbulent Aerosol fluxes from airborne measurements over the Arctic Ocean, Geophysical Research Letters, 52, e2025GL117 094, https://doi.org/10.1029/2025GL117094, 2025.

Simon, D. J., Schaefer, J., Hartmann, M., Weinhold, K., and Stratmann, F.: Airborne in-situ measurements of aerosol particle number size distributions during the BACSAM II campaign in April 2024, https://doi.org/10.1594/PANGAEA.993546, 2026.

Spreen, G., Kaleschke, L., and Heygster, G.: Sea ice remote sensing using AMSR-E 89-GHz channels, Journal of Geophysical Research: Oceans, 113, https://doi.org/10.1029/2005JC003384, 2008.

Von der Weiden, S.-L., Drewnick, F., and Borrmann, S.: Particle Loss Calculator–a new software tool for the assessment of the performance of aerosol inlet systems, Atmospheric Measurement Techniques, 2, 479–494, https://doi.org/10.5194/amt-2-479-2009, 2009.

Weber, R., Clarke, A., Litchy, M., Li, J., Kok, G., Schillawski, R., and McMurry, P.: Spurious aerosol measurements when sampling from aircraft in the vicinity of clouds, Journal of Geophysical Research: Atmospheres, 103, 28 337–28 346, https://doi.org/10.1029/98JD02086, 1998.

Willis, M. D., Köllner, F., Burkart, J., Bozem, H., Thomas, J. L., Schneider, J., Aliabadi, A. A., Hoor, P. M., Schulz, H., Herber, A. B., Leaitch, W. R., and Abbatt, J. P. D.: Evidence for marine biogenic influence on summertime Arctic aerosol, Geophysical Research Letters, 44, 6460–6470, https://doi.org/10.1002/2017GL073359, 2017.